

# Tuning electron correlation in magic-angle twisted bilayer graphene using Coulomb screening

Xiaoxue Liu<sup>1</sup>, Zhi Wang<sup>1</sup>, K. Watanabe<sup>2</sup>, T. Taniguchi<sup>2</sup>, Oskar Vafek<sup>3,4</sup>, and J.I.A. Li<sup>1†\*</sup>

<sup>1</sup>*Department of Physics, Brown University, Providence, RI 02912, USA*

<sup>2</sup>*National Institute for Materials Science, 1-1 Namiki, Tsukuba 305-0044, Japan*

<sup>3</sup>*Department of Physics, Florida State University, Tallahassee, FL 32306, USA and*

<sup>4</sup>*National High Magnetic Field Laboratory, Tallahassee, Florida, 32310, USA*

(Dated: December 22, 2024)

The ability to control the strength of interaction is essential for understanding the mechanism underlying the quantum phenomena displayed by a correlated fermionic system. For example, the isotope effect served as an important experimental support for the electron-phonon mechanism of BCS theory of superconductivity [1, 2]. In addition, the ability to tune pairing strength in a fermionic cold atom system gives rise to a unique control of the crossover between the BEC and BCS regimes, uniting the strong and weak-pairing limits [3]. In this work, we report a new device geometry where the magic-angle twisted bilayer graphene is placed in close proximity to a Bernal bilayer graphene separated by a 3 nm thick barrier. Using charge screening from the Bernal bilayer, the strength of Coulomb interaction within the twisted bilayer can be continuously tuned. This enables transport measurement to probe the role of Coulomb interaction in various emergent quantum phenomena observed in the twisted bilayer. Our results indicate that both the insulating and superconducting phases at partial filling of the moiré band become less robust as Coulomb interaction is weakened by screening. This serves as direct evidence for the role of Coulomb interaction in stabilizing the superconducting phase. In addition, the effect of Coulomb screening provides important constraints for theoretical models aiming to accurately describe the mechanism and the nature of superconductivity in magic-angle twisted bilayer graphene.

The discovery of superconductivity in magic-angle twisted bilayer graphene (tBLG) has raised intriguing questions regarding the nature of superconducting order parameter [4–6]. The coexistence of the correlated insulator (CI) and superconducting phase is compared with cuprate materials, leading to suggestions that the superconducting phase arises from an unconventional origin [4, 7–15]. On the other hand, the more recent observations of superconductivity in the absence of correlated insulator appears to indicate that superconductivity arises through the electron-phonon coupling [16, 17], an interpretation that is backed by a range of theoretical models [18–20]. However, there is little agreement upon the origin of the superconducting states despite intense effort, owing to the lack of direct experimental evidence.

It has long been recognized that the role of Coulomb interaction is essential to determining the nature of superconductivity. For a conventional superconductor, electron-phonon coupling competes against Coulomb repulsion in stabilizing superconductivity at low temperature [21, 22]. As such, a weaker Coulomb repulsion will lead to more robust superconducting order parameters. On the other hand, an unconventional superconducting phase arises from an all-electron mechanism, where the order parameter strengthens with increasing Coulomb interaction [7, 8]. While tunability in electron-phonon coupling has been demonstrated using the isotope effect [1], it remains an experimental challenge to directly control Coulomb interaction within a superconductor without introducing additional changes to the material. The flexibility of the van der Waals technique offers a unique

opportunity to control Coulomb interaction in magic-angle twisted bilayer structure using proximity screening [16, 17, 23], which promises to shed light on the nature of superconductivity.

A major road block for addressing the mechanism underlying the superconducting phase is the vastly different behavior between tBLG samples near the magic-angle, which may result from the spatial inhomogeneity of the moiré pattern [24–26]. The variation between different samples makes it difficult to provide self-consistent constraints for a theoretical model. This obstacle is addressed in this work by tuning the strength of Coulomb interaction in a single device using screening, while studying the response in both the CIs and the superconducting phase using transport measurement. We utilize a novel hybrid double-layer structure, where a Bernal bilayer graphene (BLG) and a magic-angle twisted bilayer graphene (tBLG) are separated by a thin insulating barrier with thickness of  $\xi = 3$  nm, as shown in Fig. 1a. The close proximity allows charge carriers from BLG to screen Coulomb interaction in the tBLG, offering direct control on the nature of electron correlation in the moiré flat band. Charge carrier density in BLG and tBLG,  $n_{BLG}$  and  $n_{tBLG}$ , can be independently controlled by varying the applied voltage to the top and bottom graphite gates,  $V_{top}$  and  $V_{bot}$  (see Method section for more details). A perpendicular electric field,  $D$ , can be induced by applying a voltage bias across two layers  $V_{int}$ , providing experimental control of the energy gap in BLG [27–29]. The independent control of  $n_{BLG}$ ,  $n_{tBLG}$  and  $D_{BLG}$  makes it possible to continuously vary the strength of Coulomb

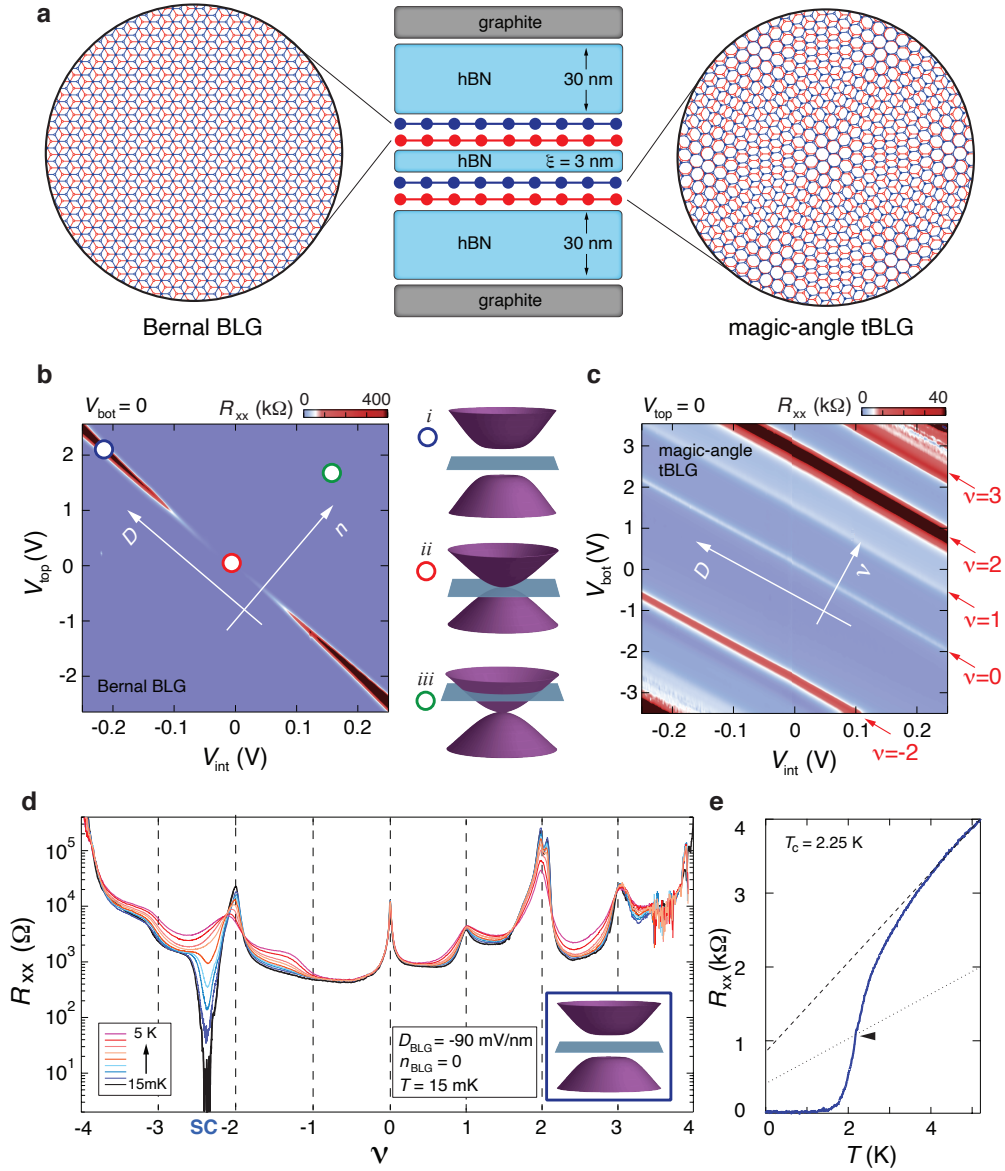


FIG. 1. **Hybrid double-layer structure with Bernal BLG and tBLG** (a) Schematic of the hybrid double-layer structure consisting of a Bernal BLG and a magic-angle tBLG, separated by a thin insulating barrier with thickness of  $\xi = 3$  nm. The structure is encapsulated with dual hexagonal boron nitride (hBN) dielectric and graphite gate electrodes. (b) Longitudinal resistance  $R_{xx}$  of Bernal BLG as a function of  $V_{top}$  and  $V_{int}$ , showing three distinct regimes of different transport behaviors, marked by red, blue and green circles. Right inset: schematic energy band structures at different combinations of  $n_{BLG}$  and  $D_{BLG}$ . (c)  $R_{xx}$  of tBLG as a function of  $V_{bot}$  and  $V_{int}$ . (d)  $R_{xx}$  as a function filling fraction in tBLG  $\nu$ , measured at  $D = -90$  mV/nm and  $n_{BLG} = 0$  with varying temperature. (e) Temperature dependence of  $R_{xx}$  for the superconducting phase at optimal doping of  $n_{tBLG} = -1.50 \times 10^{12}$  cm $^{-2}$ . The dashed line corresponds to a fit to the normal state resistance, and the dotted line 50% of normal state resistance. Transition temperature is defined at the point where  $R_{xx}$  is 50% the normal state resistance value, marked by the black arrow.

screening by changing BLG from fully insulating at large  $D_{BLG}$  and  $n_{BLG} = 0$  to highly conductive at large  $n_{BLG}$  (see supplementary information for theoretical calculation of Coulomb screening in a hybrid double-layer structure). As such, the hybrid double-layer structure provides a unique and versatile experimental platform to study and manipulate the nature of electron correlation

in the magic-angle tBLG, which promises to shed light on the underlying mechanism of the superconducting phase.

Individual components of the hybrid double-layer, BLG and tBLG, are independently characterized using transport method as a function of charge carrier density  $n$  and displacement field  $D$ . Longitudinal resistance measured from the Bernal BLG displays a well-defined

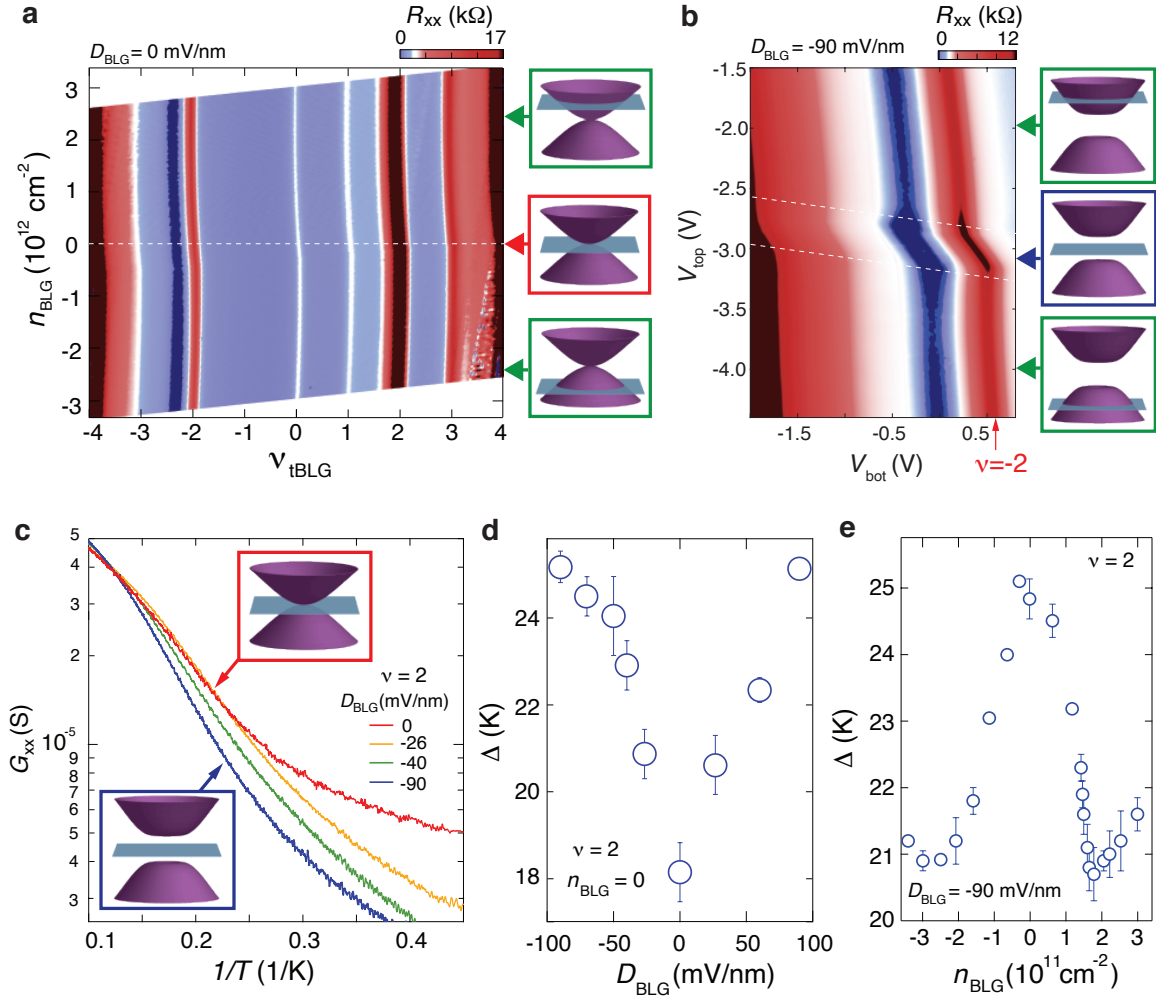


FIG. 2. **Coulomb screening and the CI** (a)  $R_{xx}$  as a function of  $\nu_{tBLG}$  and  $n_{BLG}$ , measured at  $T = 15$  mK and  $D = 0$ . The CNP in BLG is marked by the white dashed line. (b)  $R_{xx}$  as a function of  $V_{top}$  and  $V_{bot}$  near  $\nu_{tBLG} = -2$ , measured at  $T = 15$  mK and  $D_{BLG} = -90$  mV/nm. BLG is fully insulating in the density range between two white dashed lines with  $n_{BLG} = 0$ , where screening from BLG is absent and tBLG is tuned with both top and bottom graphite gate. This gives rise to the distortion in transport features. Inset in (a) and (b): schematic for energy structure of BLG at different  $n_{BLG}$  and  $D_{BLG}$ . (c) Arrhenius plot for the correlated insulating state at  $\nu = 2$ , measured at  $n_{BLG} = 0$  with varying displacement field  $D$ . (d) Activation energy gap of the  $\nu = 2$  CI state as a function of  $D_{BLG}$ . (e) Activation energy gap of the  $\nu = 2$  CI state as a function of  $n_{BLG}$ .

peak at the neutrality point which grows more insulating with increasing  $D$ -field, as shown in Fig. 1b. Three distinct regimes are identified in the parameter space which are marked by blue, red and green circles: (i) at  $n_{BLG} = 0$  and large  $D$ , a large energy gap is induced near the CNP and BLG is fully insulating (blue circle); (ii) at  $n_{BLG} = 0$  and  $D = 0$ , BLG is conductive owing to the gapless energy structure (red circle); (iii) BLG is highly conductive at large  $n_{BLG}$  (green circle). Since the strength of Coulomb screening is correlated with the conductivity of BLG, it can be continuously controlled as  $n_{BLG}$  and  $D_{BLG}$  are varied between these three regimes. The transport response of tBLG, as a function of  $D_{tBLG}$  and  $n_{tBLG}$ , is shown in Fig. 1c. The boundaries of the

moiré flat band are defined by the emergence of insulating states at  $n_{tBLG} = \pm 2.59 \times 10^{12}$  cm $^{-2}$ , which are shown at the top right and bottom left corner of Fig. 1c, indicate that the twist angle is  $\theta = 1.06^\circ$ . A normalized density scale, marked by red arrows, is defined to describe partial filling  $\nu$  of the moiré band based on the 4-fold degeneracy of spin and valley degrees of freedom for both electron and hole type carriers. Apart from the charge neutral point (CNP), a series of resistive features emerge at  $\nu = \pm 2, +1$  and  $+3$ , which are the CI states unique to the moiré flat band [4–6]. We note that the  $D$ -field has little to no consequence on the transport behavior of tBLG based on the CIs, which is consistent with the theoretical prediction of strong interlayer hybridiza-

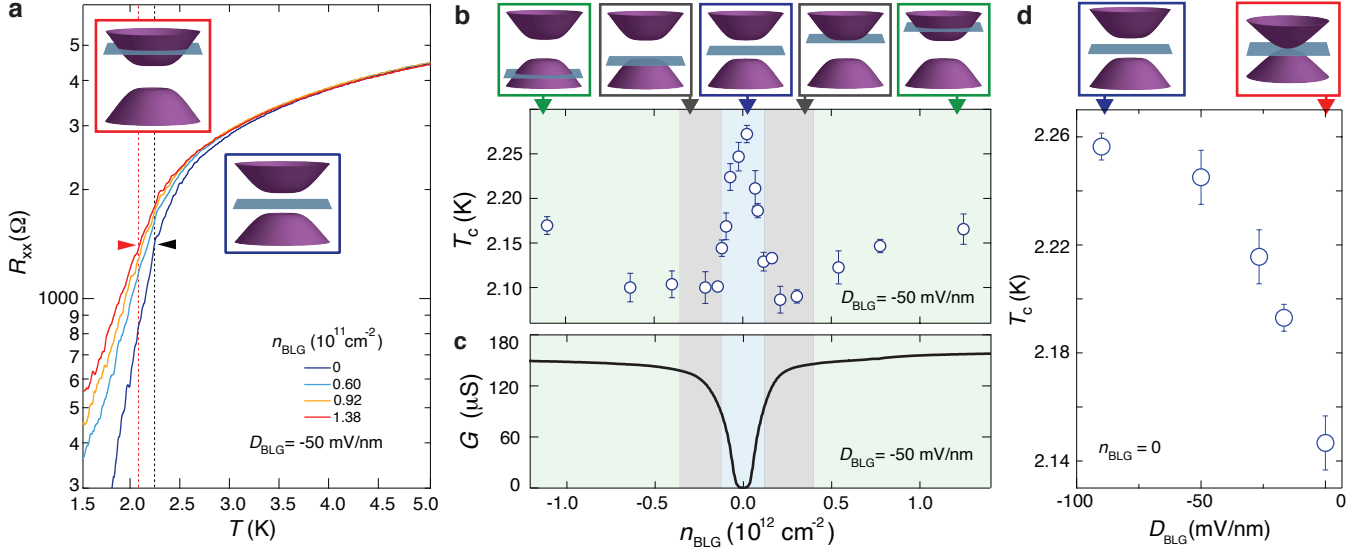


FIG. 3. **Tuning  $T_c$  of the superconducting phase** (a)  $R_{xx}$  as a function of temperature measured at optimal doping  $n_{tBLG} = -1.50 \times 10^{12} \text{ cm}^{-2}$  for different  $n_{BLG}$ .  $T_c$ , defined by 50% of normal state resistance, are marked by horizontal arrows. (b)  $T_c$  measured at optimal doping  $n_{tBLG} = -1.50 \times 10^{12} \text{ cm}^{-2}$  is plotted as a function of carrier density in BLG  $n_{BLG}$ . Top insets show the position of fermi level relative to the energy band structure at different carrier density. (c)  $R_{xx}$  in BLG as a function of carrier density  $n_{BLG}$  measured at  $D = -50 \text{ mV/nm}$ . (d)  $T_c$  as a function of  $D$  measured at optimal doping  $n_{tBLG} = -1.50 \times 10^{12} \text{ cm}^{-2}$  and  $n_{BLG} = 0$  with different  $D$ . Top insets show the schematic of band structure where an energy gap is induced by large  $D$ -field.

tion [30–32]. This insensitivity eliminates  $D$ -dependence in transport measurement arising from disorder concentrated on one graphene layer [5]. Additionally, both BLG and tBLG in the hybrid double-layer structure exhibit charge carrier inhomogeneity of  $\delta n < \pm 2 \times 10^{10}$ , measured by the divergent Hall resistance peaks at a small magnetic field  $B = 0.15 \text{ T}$ . The excellent sample quality offers a pristine environment to examine the effect of Coulomb screening with high sensitivity.

First, we examine the transport response in tBLG that is intrinsic to electron correlation within the moiré flat band, to establish a point of reference. This can be achieved by tuning BLG to be fully insulating at  $n_{BLG} = 0$  and  $D = -90 \text{ mV/nm}$ , thereby minimizing the Coulomb screening from BLG. Fig. 1d plots  $R_{xx}$  of tBLG over the full filling range of the moiré flat band, measured with varying temperature. A robust regime of superconducting phase is observed at low temperature, evidenced by  $R_{xx}$  dropping to zero within the noise band of the measurement. At the optimal doping of around  $n_{tBLG} = -1.50 \times 10^{12} \text{ cm}^{-2}$ , the transition temperature  $T_c$  is shown to be 2.25 K, Fig. 1e, which is in line with previous observation in tBLG with similar twist angle [17]. In addition, CIs exhibit thermally activated behavior. An energy gap  $\Delta$  can be extracted from the slope of the Arrhenius plot, providing a measure for the strength of the CI state. For example, the energy gap of the CI at  $\nu = 2$  is shown to be  $\Delta_{\nu=2} \sim 25 \text{ K}$  in Fig. 2c, which is significantly larger than previous observation [5, 6, 9, 16, 17],

which can be contributed to high sample quality.

The robust CI and superconducting states in Fig. 1d establish an excellent starting point, from which Coulomb screening can be introduced by tuning two independent experimental knobs: carrier density in BLG  $n_{BLG}$  and displacement field  $D_{BLG}$ . At  $D_{BLG} = 0$ , BLG is conductive over the entire density range owing to the gapless energy band. As a result, Coulomb screening from BLG remains strong and insensitive to  $n_{BLG}$ . This is confirmed in Fig. 2a, where the transport behavior of the CI and the superconducting phase exhibit no change over a large range of  $n_{BLG}$  (see Fig. SI9 for  $\Delta_{\mu=2}$  as a function of the  $n_{BLG}$  at  $D_{BLG} = 0$ ). On the other hand, Fig. 2b shows that the effect of Coulomb screening can be sensitively controlled with  $n_{BLG}$  at large  $D_{BLG}$ : the CIs is more resistive and a larger superconducting regime is observed when BLG is fully insulating with fermi level lying inside the energy gap induced by  $D_{BLG}$ . In the following, we will quantitatively examine the effect of Coulomb screening on both the CI and the superconducting phase, by studying the dependence of transport behavior on  $D_{BLG}$  and  $n_{BLG}$ . It is worth noting that controlling  $n_{BLG}$  and  $D_{BLG}$  have different effects on the nature of Coulomb screening (see SI for more detailed discussion). Therefore, studying the influence of both parameters promises to provide a more thorough characterization for the nature of correlation in tBLG.

Fig. 2c-e examine the evolution of the CI while Coulomb screening is being modified by varying  $D_{BLG}$

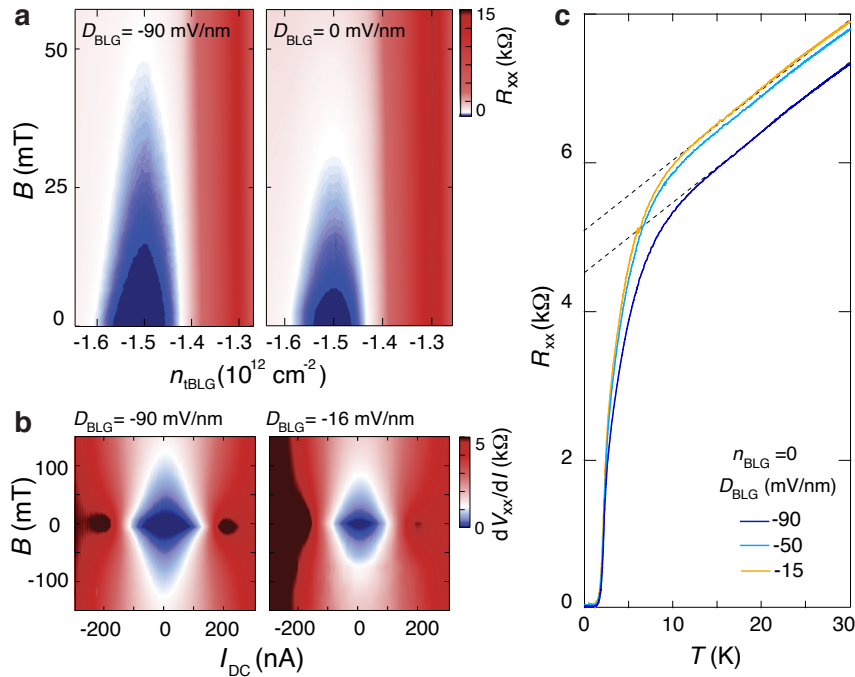


FIG. 4.  **$B$ -field and current dependence, normal state resistance** (a)  $R_{xx}$  as a function of carrier density in tBLG,  $n_{tBLG}$ , and magnetic field  $B$ . BLG is tuned to  $n_{BLG} = 0$  with  $D_{BLG} = -90$  mV/nm (left panel) and 0 (right panel). (b) Critical current as a function of magnetic field measured at optimal doping  $n_{tBLG} = -1.50 \times 10^{12}$  cm $^{-2}$ . BLG is tuned to  $n_{BLG} = 0$  with  $D_{BLG} = -90$  mV/nm (left panel) and  $-16$  mV/nm (right panel). (c)  $R_{xx}$  as a function of  $T$  measured at optimal doping, showing a linear in  $T$  behavior at  $T > T_c$  at  $n_{BLG} = 0$  with varying  $D_{BLG}$ .

and  $n_{BLG}$ . The temperature dependence of  $R_{xx}$  at  $\nu = 2$  exhibits thermally activated behavior with strong  $D_{BLG}$  dependence, as shown in Fig. 2c. Over the temperature range in Fig. 2c, BLG remains insulating at  $n_{BLG} = 0$  and  $D_{BLG} \neq 0$ , ensuring that the strength of Coulomb screening from BLG is controlled only by  $D_{BLG}$  while remaining insensitive to temperature (see SI for temperature dependence of transport response in BLG). Fig. 2d demonstrates that the energy gap  $\Delta_{\nu=2}$  is larger when BLG is more insulating at larger  $D_{BLG}$ . Similar behavior in  $\Delta_{\nu=2}$  is observed as a function of  $n_{BLG}$  in Fig. 2e. Since CIs at integer filling arise from Coulomb correlation within the moiré flat band [9, 30, 33, 34], the trend in  $\Delta_{\nu=2}$  provides strong evidence that electron correlation in tBLG is directly tunable using Coulomb screening in a double-layer structure: screening from the BLG decreases as BLG becomes less conductive, leading to stronger Coulomb interaction and an enhanced energy gap for the CI states. Not only does this observation show excellent agreement with theoretical models regarding the effect of Coulomb screening (see SI for more detailed theoretical discussion), it provides an important reference for studying the nature of superconductivity in tBLG using Coulomb screening from BLG.

The observations in Fig. 2d-e have a few important implications: (i) Fig. 2d shows that  $\Delta_{\nu=2}$  is symmetric around  $D = 0$ , which eliminates the more trivial expla-

nation that the  $D$ -dependence in  $\Delta_{\nu=2}$  arises from inhomogeneous distribution of disorder across two graphene layers; (ii) a minimum in  $\Delta_{\nu=2}$  is observed in Fig. 2e near the band edge of BLG,  $n_{BLG} \sim 2 \times 10^{11}$  cm $^{-2}$ . This suggests that Coulomb screening is the strongest when the fermi level of BLG is near the van Hove singularities where the density of states is the largest [35, 36]; (iii) the value of  $\Delta_{\nu=2}$  remains large in the presence of strong Coulomb screening, suggesting that the CI cannot be fully suppressed by Coulomb screening alone [16].

Having established the effect of Coulomb screening on CIs, we turn our attention to the superconducting phase in tBLG. The temperature dependence of  $R_{xx}$  near the transition exhibits an apparent shift with varying carrier density in BLG  $n_{BLG}$ , while the normal state resistance at  $T > T_c$  remains unchanged, as shown in Fig. 3a. This indicates that Coulomb screening directly couples to the underlying mechanism of superconductivity. Fig. 3b and c show that  $T_c$  as a function of  $n_{BLG}$  closely follows the conductance of BLG:  $T_c$  is enhanced (suppressed) when BLG is fully insulating (conductive). Similar behavior in  $T_c$  is observed when Coulomb screening is tuned with varying  $D$  field at  $n_{BLG} = 0$ . Starting from  $D = -90$  mV/nm and  $n_{BLG} = 0$ ,  $T_c$  is increasingly suppressed with decreasing  $D$  as the energy gap of BLG near the CNP becomes smaller, as shown in Fig. 3d (see SI for the evolution of energy gap in BLG versus  $D_{BLG}$ ). Since

Coulomb screening is stronger (weaker) when BLG is more conductive (insulating), the trend in  $T_c$  as a function of  $n_{BLG}$  and  $D_{BLG}$  indicates that a more robust superconducting phase results from stronger Coulomb correlation within the tBLG. We note that the trend in  $T_c$  is insensitive to the detail of how  $T_c$  is defined, given the systematic shift in the temperature dependence of  $R_{xx}$  (see SI for comparison between the shift in  $R_{xx}$  induced by varying  $D_{BLG}$  and  $n_{BLG}$ ). Interestingly,  $T_c$  is suppressed the most as BLG transitions from fully insulating to conductive with increasing carrier density. A similar response near the band edge of BLG provides further evidence that changes in  $\Delta_{\nu=2}$  of the CI and  $T_c$  of the superconducting phase both result from the influence of Coulomb screening. In addition, it confirms that the effect of Coulomb screening is the strongest in the presence of large density of states in the screening layer.

Apart from transition temperature  $T_c$ , the magnetic field  $B$  and current bias  $I$  dependence of the superconducting phase offers further characterization for the effect of Coulomb screening. Fig. 4a plots the density-magnetic field phase diagram, where the superconducting phase is shown as dark blue in the chosen color scale. When BLG is conductive at  $D = 0$ , both the density and  $B$ -field range for the superconducting phase is reduced as compared to  $n_{BLG} = 0$  and  $D = -90$  mV/nm, where the BLG is fully insulating. Similarly, the critical current of the superconducting phase at optimal doping is reduced at smaller  $D$  compared to  $D = -90$  mV/nm, as shown in Fig. 4b. The magnetic field and current bias dependence provide a more thorough characterization of the superconducting phase, confirming the role of Coulomb interaction in stabilizing superconductivity in tBLG.

Lastly, we examine the influence of Coulomb screening on the normal state resistance in tBLG. Above the transition temperature  $T_c$ , Fig. 4c shows that  $R_{xx}$  at optimal doping exhibits linear-in- $T$  behavior over a large temperature range,  $10 < T < 30$  K. Most intriguingly, the slope of  $R_{xx}$  in the  $T$ -linear regime remains constant as the strength of Coulomb screening is modified by varying  $D_{BLG}$  and  $n_{BLG}$  (Also see Fig. SI8). It has been suggested that the slope of the  $T$ -linear regime is associated with the strength of quasielastic electron scattering off acoustic phonon modes [37, 38]. Within this interpretation, the constant slope would indicate that the strength of acoustic electron-phonon coupling is not influenced by Coulomb screening.

Taken together, our results provide several important constraints for theoretical models aiming to accurately describe superconductivity in magic-angle tBLG. The effect of Coulomb screening described in this work seems to point towards superconductivity driven purely by Coulomb forces among electrons, although we cannot exclude an electron-phonon mechanism, with the superconducting order parameter somehow strengthened by the Coulomb interaction. In addition, we note that the influ-

ence of Coulomb screening is quantitatively stronger on the relative increase of the energy gap of CI ( $\sim 20-30\%$ ) compared to the relative increase of  $T_c$  of the superconductor ( $\sim 6-7\%$ ). Understanding this quantitative difference is an open challenge for theory.

## ACKNOWLEDGMENTS

We thank M. Yankowitz, A. F. Young, C. R. Dean, Q. Shi for discussions and Y. Zeng for helpful input on fabrication. This work was primarily supported by Brown University. Device fabrication was performed in the Institute for Molecular and Nanoscale Innovation at Brown University. O. V. was supported by NSF DMR-1916958, and by the National High Magnetic Field Laboratory through NSF Grant No. DMR-1157490 and the State of Florida. K.W. and T.T. acknowledge support from the EMEXT Element Strategy Initiative to Form Core Research Center, Grant Number JPMXP0112101001 and the CREST(JPMJCR15F3), JST.

## COMPETING FINANCIAL INTERESTS

The authors declare no competing financial interests.

---

\* jia.li@brown.edu

- [1] E. Maxwell, Phys. Rev. **78**, 477 (1950).
- [2] J. Bardeen, L. N. Cooper, and J. R. Schrieffer, Phys. Rev. **108**, 1175 (1957).
- [3] M. Randeria and E. Taylor, Annual Review of Condensed Matter Physics **5**, 209 (2014).
- [4] Y. Cao, V. Fatemi, S. Fang, K. Watanabe, T. Taniguchi, E. Kaxiras, and P. Jarillo-Herrero, Nature **556**, 43 (2018).
- [5] M. Yankowitz, S. Chen, H. Polshyn, Y. Zhang, K. Watanabe, T. Taniguchi, D. Graf, A. F. Young, and C. R. Dean, Science **363**, 1059 (2019).
- [6] X. Lu, P. Stepanov, W. Yang, M. Xie, M. A. Aamir, I. Das, C. Urgell, K. Watanabe, T. Taniguchi, G. Zhang, A. Bachtold, A. H. MacDonald, and D. K. Efetov, arXiv preprint arXiv:1903.06513 (2019).
- [7] B. Keimer, S. A. Kivelson, M. R. Norman, S. Uchida, and J. Zaanen, Nature **518**, 179 (2015).
- [8] P. A. Lee, N. Nagaosa, and X.-G. Wen, Rev. Mod. Phys. **78**, 17 (2006).
- [9] Y. Cao, V. Fatemi, A. Demir, S. Fang, S. L. Tomarken, J. Y. Luo, J. D. Sanchez-Yamagishi, K. Watanabe, T. Taniguchi, E. Kaxiras, R. C. Ashoori, and P. Jarillo-Herrero, Nature **556**, 80 (2018).
- [10] Y. Cao, D. Chowdhury, D. Rodan-Legrain, O. Rubies-Bigorda, K. Watanabe, T. Taniguchi, T. Senthil, and P. Jarillo-Herrero, Physical Review Letters **124**, 076801 (2020).
- [11] C. Xu and L. Balents, Physical review letters **121**, 087001 (2018).



- [12] H. Isobe, N. F. Yuan, and L. Fu, arXiv preprint arXiv:1805.06449 (2018).
- [13] H. Guo, X. Zhu, S. Feng, and R. T. Scalettar, Physical Review B **97**, 235453 (2018).
- [14] S. Ray, J. Jung, and T. Das, Phys. Rev. B **99**, 134515 (2019).
- [15] D. V. Chichinadze, L. Classen, and A. V. Chubukov, “Nematic superconductivity in twisted bilayer graphene,” (2019), arXiv:1910.07379 [cond-mat.supr-con].
- [16] P. Stepanov, I. Das, X. Lu, A. Fahimniya, K. Watanabe, T. Taniguchi, F. H. Koppens, J. Lischner, L. Levitov, and D. K. Efetov, arXiv preprint arXiv:1911.09198 (2019).
- [17] Y. Saito, J. Ge, K. Watanabe, T. Taniguchi, and A. F. Young, arXiv preprint arXiv:1911.13302 (2019).
- [18] M. Ochi, M. Koshino, and K. Kuroki, Phys. Rev. B **98**, 081102 (2018).
- [19] B. Lian, Z. Wang, and B. A. Bernevig, Phys. Rev. Lett. **122**, 257002 (2019).
- [20] F. Wu, A. H. MacDonald, and I. Martin, Phys. Rev. Lett. **121**, 257001 (2018).
- [21] W. L. McMillan, Phys. Rev. **167**, 331 (1968).
- [22] P. B. Allen and R. C. Dynes, Phys. Rev. B **12**, 905 (1975).
- [23] J. M. Pizarro, M. Rösner, R. Thomale, R. Valentí, and T. O. Wehling, Phys. Rev. B **100**, 161102 (2019).
- [24] H. Yoo, R. Engelke, S. Carr, S. Fang, K. Zhang, P. Cazeaux, S. H. Sung, R. Hovden, A. W. Tsen, T. Taniguchi, *et al.*, Nature materials **18**, 448 (2019).
- [25] L. McGilly, A. Kerelsky, N. Finney, K. Shapovalov, E.-M. Shih, A. Ghiotto, Y. Zeng, S. Moore, W. Wu, Y. Bai, *et al.*, arXiv preprint arXiv:1912.06629 (2019).
- [26] A. Uri, S. Grover, Y. Cao, J. Crosse, K. Bagani, D. Rodan-Legrain, Y. Myasoedov, K. Watanabe, T. Taniguchi, P. Moon, *et al.*, arXiv preprint arXiv:1908.04595 (2019).
- [27] Y. Zhang, T.-T. Tang, C. Girit, Z. Hao, M. C. Martin, A. Zettl, M. F. Crommie, Y. R. Shen, and F. Wang, Nature **116**, 136802 (2009).
- [28] J. I. A. Li, C. Tan, S. Chen, Y. Zeng, T. Taniguchi, K. Watanabe, J. Hone, and C. R. Dean, Science **358**, 648 (2017).
- [29] A. A. Zibrov, C. R. Kometter, H. Zhou, E. M. Spanton, T. Taniguchi, K. Watanabe, M. P. Zaletel, and A. F. Young, Nature **549**, 360 (2017).
- [30] R. Bistritzer and A. H. MacDonald, Proceedings of the National Academy of Sciences **108**, 12233 (2011).
- [31] G. Trambly de Laissardière, O. F. Namarvar, D. Mayou, and L. Magaud, Phys. Rev. B **93**, 235135 (2016).
- [32] K. Kim, A. DaSilva, S. Huang, B. Fallahazad, S. Larentis, T. Taniguchi, K. Watanabe, B. J. LeRoy, A. H. MacDonald, and E. Tutuc, Proceedings of the National Academy of Sciences **114**, 3364 (2017).
- [33] C. Wu, D. Bergman, L. Balents, and S. Das Sarma, Phys. Rev. Lett. **99**, 070401 (2007).
- [34] J. Kang and O. Vafek, Phys. Rev. Lett. **122**, 246401 (2019).
- [35] A. F. Young and L. S. Levitov, Phys. Rev. B **84**, 085441 (2011).
- [36] B. M. Hunt, J. I. A. Li, A. A. Zibrov, L. Wang, T. Taniguchi, K. Watanabe, J. Hone, C. R. Dean, M. Zaletel, R. C. Ashoori, and A. F. Young, Nature Communications **8**, 948 (2017).
- [37] F. Wu, E. Hwang, and S. Das Sarma, Phys. Rev. B **99**, 165112 (2019).
- [38] H. Polshyn, M. Yankowitz, S. Chen, Y. Zhang, K. Watanabe, T. Taniguchi, C. R. Dean, and A. F. Young, Nature Physics, **1** (2019).
- [39] E. McCann, Phys. Rev. B **74**, 161403 (2006).
- [40] K. Kim, M. Yankowitz, B. Fallahazad, S. Kang, H. C. Movva, S. Huang, S. Larentis, C. M. Corbet, T. Taniguchi, K. Watanabe, *et al.*, Nano letters **16**, 1989 (2016).

SUPPLEMENTARY MATERIAL

Screening of the Coulomb interaction due to the Bernal bilayer

The interaction among the electrons in the twisted bilayer is modified due to the presence of the Bernal bilayer. The Hamiltonian for the combined system is

$$H_{int} = \int d^2\mathbf{r} \int d^2\mathbf{r}' \left( \frac{1}{2}n_1(\mathbf{r})V^{\parallel}(\mathbf{r}-\mathbf{r}')n_1(\mathbf{r}') + \frac{1}{2}n_2(\mathbf{r})V^{\parallel}(\mathbf{r}-\mathbf{r}')n_2(\mathbf{r}') + n_1(\mathbf{r})V^{\perp}(\mathbf{r}-\mathbf{r}')n_2(\mathbf{r}') \right), \quad (1)$$

where  $\mathbf{r}$  and  $\mathbf{r}'$  are 2D position vectors,  $n_1(\mathbf{r})$  is the electron density in the twisted bilayer, and  $n_2(\mathbf{r})$  is the electron density in the Bernal bilayer. The intra-layer Coulomb interaction is

$$V^{\parallel}(\mathbf{r}) = \frac{e^2}{|\mathbf{r}|} = \int \frac{d^2\mathbf{q}}{(2\pi)^2} \frac{2\pi e^2}{|\mathbf{q}|} e^{i\mathbf{q}\cdot\mathbf{r}}, \quad (2)$$

and the inter-layer Coulomb interaction for the two layers separated by distance  $\xi$  is

$$V^{\perp}(\mathbf{r}) = \frac{e^2}{\sqrt{\mathbf{r}^2 + \xi^2}} = \int \frac{d^2\mathbf{q}}{(2\pi)^2} \frac{2\pi e^2}{|\mathbf{q}|} e^{-|\mathbf{q}|\xi} e^{i\mathbf{q}\cdot\mathbf{r}}. \quad (3)$$

To find the effective interaction within the twisted bilayer, we write the coherent state Feynman path integral action corresponding to  $H_{int}$ , Hubbard-Stratonovic decouple the intra-layer interaction in the Bernal bilayer, and integrate out the fermions in the Bernal bilayer and expand the result to quadratic order. Finally, we integrate out the Hubbard-Stratonovic field and obtain the static interaction

$$V^{eff}(\mathbf{r}) = \int \frac{d^2\mathbf{q}}{(2\pi)^2} \frac{2\pi e^2}{|\mathbf{q}|} \left( 1 - e^{-2|\mathbf{q}|\xi} \left( 1 - \frac{1}{\epsilon_{AB}(\mathbf{q})} \right) \right) e^{i\mathbf{q}\cdot\mathbf{r}}, \quad (4)$$

where the  $\mathbf{q}$ -dependent dielectric constant of the Bernal bilayer can be related to its static polarization function  $\Pi_{\mathbf{q}}^0$  as  $\epsilon_{AB}(\mathbf{q}) = 1 + \frac{2\pi e^2}{|\mathbf{q}|} \Pi_{\mathbf{q}}^0$ .

To gain a qualitative understanding of the above result, consider first the case when the Bernal bilayer is gated to a finite carrier density and thus acts as a metal. Then,  $\Pi_{\mathbf{q}\rightarrow 0}^0 \rightarrow const.$  and the dielectric constant diverges as  $\mathbf{q} \rightarrow 0$ . The effective interaction potential in momentum space then precisely corresponds to the real space potential produced by the test charge and its mirror image a distance  $2\xi$  above the twisted bilayer as it should. On the other hand, when the Bernal bilayer is insulating,  $\Pi_{\mathbf{q}\rightarrow 0}^0 \sim \mathbf{q}^2$  and the long distance effective interaction is unchanged by the presence of the Bernal bilayer.

A more quantitative determination of the  $V^{eff}(\mathbf{r})$  requires a microscopic calculation of  $\Pi_{\mathbf{q}}^0$ . We start with the low energy Hamiltonian for the electrons near the two valleys[39] labeled by  $\tau_z = \pm 1$  acting on the basis  $(\psi_{B2}, \psi_{A1}, \psi_{B1}, \psi_{A2})$  as

$$\mathcal{H}_{AB}(\mathbf{p}) = \tau_z \begin{pmatrix} -\frac{1}{2}\Delta & 0 & 0 & v_F(p_x - ip_y) \\ 0 & \frac{1}{2}\Delta & v_F(p_x + ip_y) & 0 \\ 0 & v_F(p_x - ip_y) & \frac{1}{2}\Delta & \tau_z \gamma_1 \\ v_F(p_x + ip_y) & 0 & \tau_z \gamma_1 & -\frac{1}{2}\Delta \end{pmatrix}. \quad (5)$$

For polarization function we need

$$\Pi_{\mathbf{q}}^0(\Omega) = -k_B T \sum_{\omega_n} \int \frac{d^2\mathbf{k}}{(2\pi)^2} \text{Tr} (G_{\mathbf{k}+\mathbf{q}}(\omega_n + \Omega_n) G_{\mathbf{k}}(\omega_n)), \quad (6)$$

where the Matsubara frequency  $\omega_n = (2n+1)\pi k_B T$  and the matrix Green's function is

$$G_{\mathbf{k}}(\omega_n) = (-i\omega_n 1_4 + \mathcal{H}_{AB}(\mathbf{k}))^{-1}. \quad (7)$$

Because the  $\mathcal{H}_{AB}^2$  is more easily invertable, we can find the  $G_{\mathbf{k}}(\omega_n)$  by first inverting  $\omega_n^2 + \mathcal{H}_{AB}^2$  and then left multiplying the result by  $i\omega_n + \mathcal{H}_{AB}$ . We find

$$G_{\mathbf{p}}(\omega) = \sum_{s=\pm} \frac{i\omega 1_4 + \mathcal{H}_{AB}(\mathbf{p})}{\omega^2 + E_s^2(\mathbf{p})} \Lambda_s(\mathbf{p}), \quad (8)$$



where the four eigenenergies are

$$E_s(\mathbf{p}) = \pm \sqrt{\left(\frac{\Delta^2}{4} + \frac{\gamma_1^2}{2} + v_F^2 \mathbf{p}^2\right) + s \sqrt{\frac{\gamma_1^4}{4} + (\gamma_1^2 + \Delta^2)v_F^2 \mathbf{p}^2}}, \quad (9)$$

for  $s = \pm 1$ , and

$$\Lambda_s(\mathbf{p}) = \frac{1}{2} \left( 1_4 - \frac{s}{\sqrt{\frac{\gamma_1^4}{4} + (\gamma_1^2 + \Delta^2)v_F^2 \mathbf{p}^2}} \begin{pmatrix} \frac{\gamma_1^2}{2} & -v_F \mathbf{p} \cdot \boldsymbol{\sigma} (\gamma_1 \tau_z \sigma_1 + \Delta \sigma_3) \\ -(\gamma_1 \tau_z \sigma_1 + \Delta \sigma_3) v_F \mathbf{p} \cdot \boldsymbol{\sigma} & -\frac{\gamma_1^2}{2} \end{pmatrix} \right). \quad (10)$$

Finally, including the spin and valley degeneracy:

$$\Pi_{\mathbf{q}}^0 = \sum_{\tau_z = \pm} \sum_{s_1, s'_1 = \pm} \sum_{s_2, s'_2 = \pm} \int \frac{d^2 \mathbf{p}}{(2\pi \hbar)^2} \frac{\tanh\left(\frac{s'_1 E_{s_1}(\mathbf{p} + \mathbf{q}) - \mu}{2k_B T}\right) - \tanh\left(\frac{s'_2 E_{s_2}(\mathbf{p}) - \mu}{2k_B T}\right)}{s'_1 E_{s_1}(\mathbf{p} + \mathbf{q}) - s'_2 E_{s_2}(\mathbf{p})} \text{Tr} [P_{s_1, s'_1}(\mathbf{p} + \mathbf{q}) P_{s_2, s'_2}(\mathbf{p})], \quad (11)$$

where the projector on the individual eigenstates is

$$P_{s, s'}(\mathbf{p}) = \frac{1}{2} \left( 1 + s' \frac{\mathcal{H}_{AB}(\mathbf{p})}{E_s(\mathbf{p})} \right) \Lambda_s(\mathbf{p}). \quad (12)$$

We can rescale all the energies by  $\gamma_1$  which allows us to rewrite the polarization function via a scaling function  $\Phi$  as

$$\Pi_{\mathbf{q}}^0 = \frac{\gamma_1}{\hbar^2 v_F^2} \Phi \left( \frac{\hbar v_F q}{\gamma_1}, \frac{\Delta}{\gamma_1}, \frac{\mu}{\gamma_1}, \frac{k_B T}{\gamma_1} \right). \quad (13)$$

We determine  $\Phi$  by numerically performing the integral (11). The static dielectric function is then

$$V_{\mathbf{q}} \Pi_{\mathbf{q}}^0(0) = 2\pi \frac{e^2}{\epsilon_{hBN} |\mathbf{q}| \hbar^2 v_F^2} \Phi \left( \frac{\hbar v_F q}{\gamma_1}, \frac{\Delta}{\gamma_1}, \frac{\mu}{\gamma_1}, \frac{k_B T}{\gamma_1} \right) = \frac{2\pi}{\epsilon_{hBN}} \times \frac{c}{v_F} \times \frac{e^2}{\hbar c} \times \frac{\gamma_1}{\hbar v_F q} \Phi \left( \frac{\hbar v_F q}{\gamma_1}, \frac{\Delta}{\gamma_1}, \frac{\mu}{\gamma_1}, \frac{k_B T}{\gamma_1} \right). \quad (14)$$

Writing the exponential screening factor in Eqn.(4) using scaling variables, we get  $e^{-2|\mathbf{q}|\xi} = \exp\left(-\left(\frac{\hbar v_F q}{\gamma_1}\right)\left(2\frac{\gamma_1 \xi}{\hbar v_F}\right)\right)$ . For  $\xi = 3\text{nm}$ ,  $\gamma_1 = 0.3\text{eV}$ , and  $v_F = 10^6\text{m/s}$ , we have  $2\frac{\gamma_1 \xi}{\hbar v_F} = 2.735$ ; we also set  $\epsilon_{hBN} = 4.4$ . In the Figure 1 we place the chemical potential  $\mu$  at the CNP and vary the gap  $\Delta$  of the Bernal bilayer from 0meV to 30meV. We see that the reduction of the repulsive interaction in the twisted bilayer is minimized when the CNP gap of the Bernal bilayer is maximized. In Figure 2 we set  $\Delta = 30\text{meV}$  and vary the carrier concentration, moving the chemical potential from the middle of the gap to 15meV above the conduction band minimum. We see that the reduction of the repulsive interaction in the twisted bilayer is minimized when the chemical potential sits in the gap of the Bernal bilayer. We also see that the interaction is almost independent of the filling of the Bernal bilayer once it is conducting. Remarkably, the maximal increase in the superconducting  $T_c$  as well as the gap of the correlated insulator correspond to the strongest Coulomb repulsion  $V_{\mathbf{q}}^{eff}$  i.e. the minimal reduction of  $V_{\mathbf{q}}^{\parallel}$ .

### Sample fabrication

The tBLG in the hybrid double-layer structure is assembled using the ‘‘cut-and-stack’’ technique [17], instead of the ‘‘tear-and-stack’’ technique [9, 40]. All components of the structure are assembled from top to bottom using the same poly(bisphenol A carbonate) (PC)/polydimethylsiloxane (PDMS) stamp mounted on a glass slide. The sequence of stacking is: graphite as top gate electrode, 30 nm thick hBN as top dielectric, Bernal bilayer graphene, 3 nm thick hBN as insulating barrier, magic-angle tBLG, 30 nm thick hBN as bottom dielectric, bottom graphite as bottom gate electrode. The entire structure is deposited onto a doped Si/SiO<sub>2</sub> substrate, as shown in Fig.SI 3a. Electrical contact to both Bernal and twisted bilayers are made independently by CHF<sub>3</sub>/O<sub>2</sub> etching and deposition of the Cr/Au (2/100 nm) metal edge contact.

The hybrid double-layer sample is shaped into an aligned Hall bar geometry. In this geometry, each layer has independent electrical contact for longitudinal and Hall voltage measurements, as shown in Fig.SI 3b.

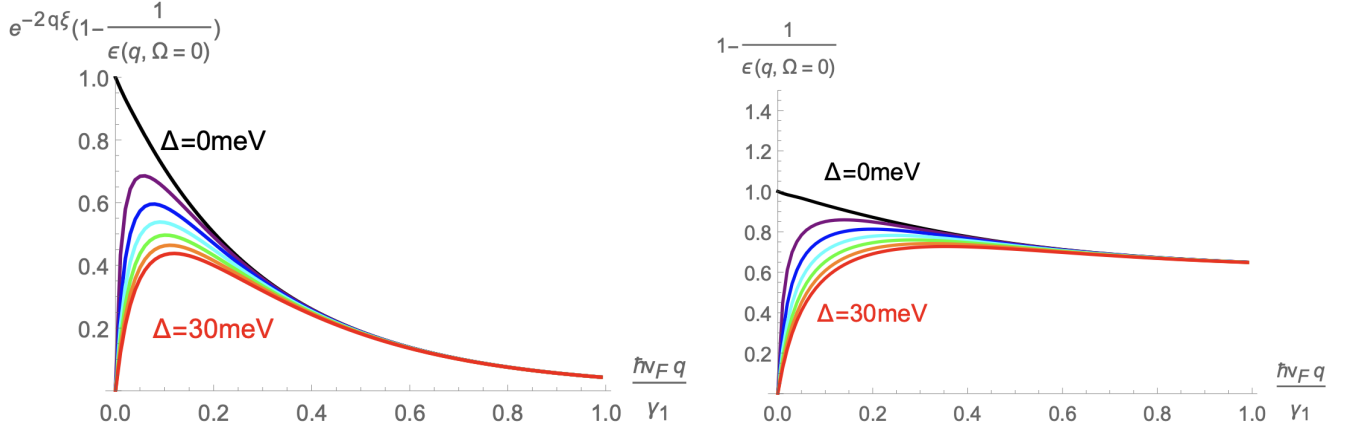


Fig.SI 1. The effective interaction among the electrons in the twisted bilayer due to static screening within the AB stacked Bernal bilayer is  $V_{\mathbf{q}}^{eff} = V_{\mathbf{q}}^{\parallel} \left(1 - e^{-2|\mathbf{q}|\xi} \left(1 - \frac{1}{\epsilon_{AB}(\mathbf{q})}\right)\right)$ . Left panel: the reduction factor as a function of dimensionless wavevector  $q$  at low temperature;  $\gamma_1 \approx 0.3\text{eV}$  is the direct interlayer tunneling defined in Eqn.(5). The series of curves shows the evolution from semimetallic Bernal bilayer  $\Delta = 0$  (top curve) to progressively more insulating Bernal bilayer as  $\Delta$  is varied in steps of 5meV, ending with the Bernal gap at 30meV (bottom curve). Right panel: The dielectric reduction factor without the exponential.

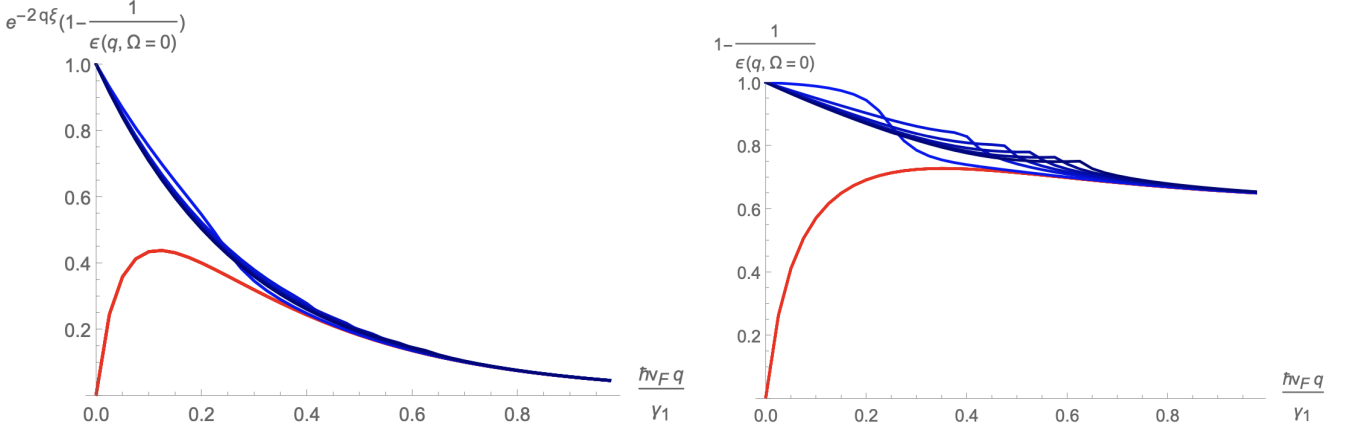


Fig.SI 2. The effective interaction among the electrons in the twisted bilayer due to static screening within the AB stacked Bernal bilayer is  $V_{\mathbf{q}}^{eff} = V_{\mathbf{q}}^{\parallel} \left(1 - e^{-2|\mathbf{q}|\xi} \left(1 - \frac{1}{\epsilon_{AB}(\mathbf{q})}\right)\right)$ . Left panel: the reduction factor as a function of dimensionless wavevector  $q$  at low temperature compared to the gap. The series of curves shows the evolution from the insulating Bernal bilayer (red curve) to conducting (blue), as the chemical potential is varied in steps of 3meV, starting from being in the middle of the Bernal gap (set to 30meV), to being 15meV above. Right panel: the dielectric reduction factor without the exponential; the  $2k_F$  features in the metallic curves are also visible.

### Transport measurement

The device geometry of the hybrid double-layer structure allows independent control of carrier density in Bernal BLG and tBLG,  $n_{BLG}$  and  $n_{tBLG}$ , as well as displacement field  $D$ . Such control is achieved by applying a DC gate voltage to top graphite electrode  $V_{top}$ , bottom graphite electrode  $V_{bot}$ , along with a voltage bias between BLG and tBLG  $V_{int}$ .  $n_{BLG}$ ,  $n_{tBLG}$  and  $D$  can be obtained using the following equations:

$$n_{BLG} = (C_{top}V_{top} + C_{int}V_{int})/e + n_{BLG}^0, \quad (15)$$

$$D_{BLG} = (C_{top}V_{top} - C_{int}V_{int})/\epsilon_0, \quad (16)$$

$$n_{tBLG} = (C_{bot}V_{bot} + C_{int}V_{int})/e + n_{tBLG}^0, \quad (17)$$

$$D_{tBLG} = (-C_{bot}V_{bot} + C_{int}V_{int})/\epsilon_0, \quad (18)$$

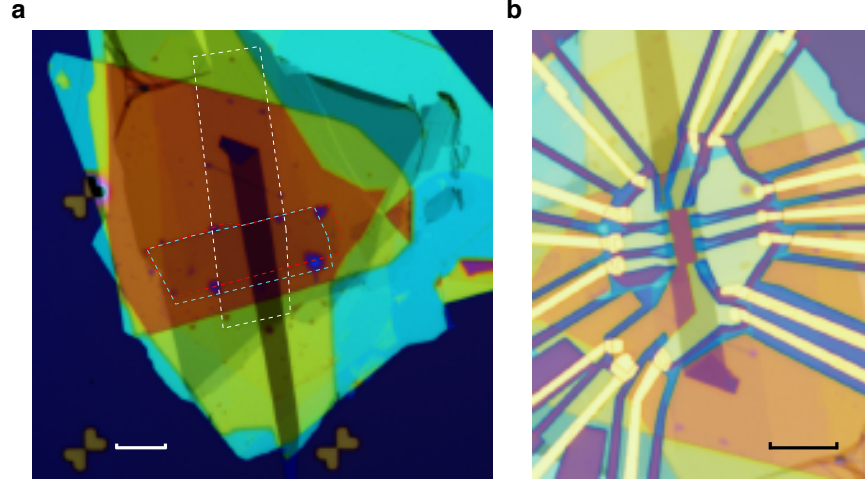


Fig.SI 3. Optical image of the hybrid double-layer structure (a) before and (b) after nanofabrication. The Bernal bilayer graphene layer is highlighted by the white dashed contour, whereas two graphene layers in tBLG are highlighted by the red and blue contours, respectively. The scale bars correspond to  $10\mu\text{m}$ .

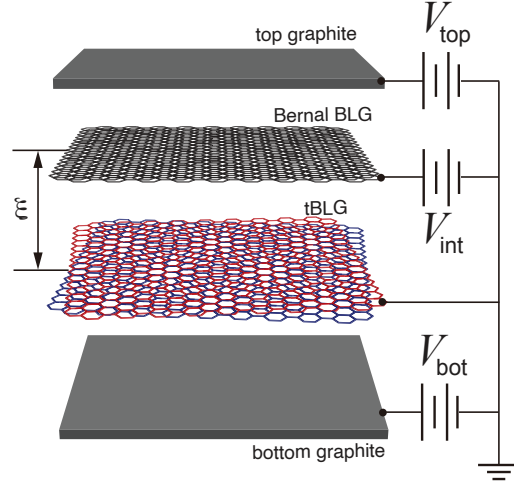


Fig.SI 4. **Schematic diagram for transport measurement** Transport measurement is performed with DC voltage bias applied to top graphite, bottom graphite and Bernal BLG, to control charge carrier density in BLG and tBLG, as well as displacement field  $D$ .

where  $C_{top}$  is the geometric capacitance between top graphite and BLG,  $C_{bot}$  the geometric capacitance between bottom graphite and tBLG, and  $C_{int}$  the geometric capacitance between BLG and tBLG.  $n_{BLG}^0$  and  $n_{tBLG}^0$  are intrinsic doping in BLG and tBLG, respectively.

Transport measurement is performed in a BlueFors LD400 dilution refrigerator with a base temperature of 15 mK. Temperature is measured using a resistance thermometer located on the sample probe. Standard low frequency lock-in techniques with Stanford Research SR830 amplifier are used to measure resistance  $R_{xx}$  and  $R_{xy}$ , with an excitation current of 0.6 – 1 nA at a frequency of 17.77 – 43.33 Hz.

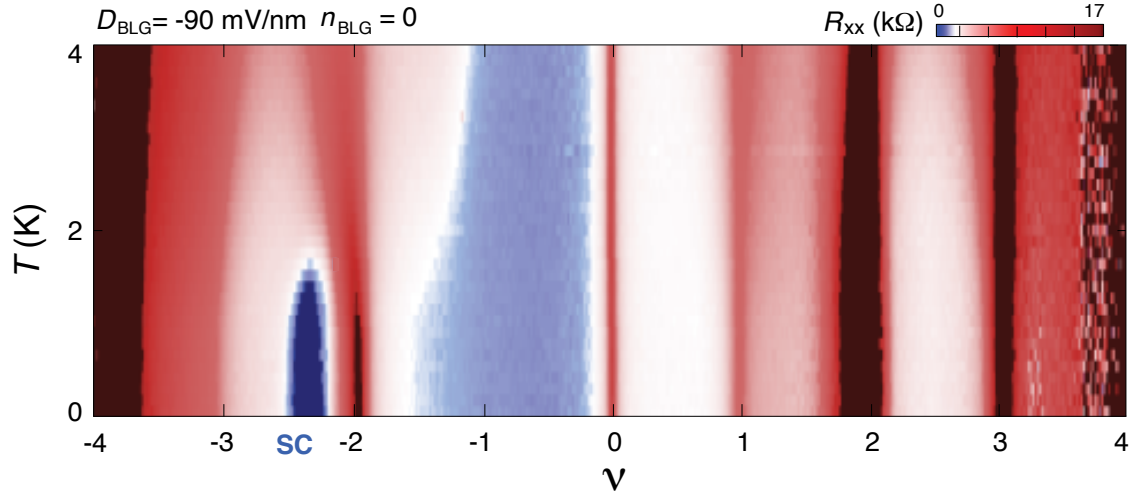


Fig.SI 5.  $R_{xx}$  versus  $\nu_{tBLG}$  and  $T$  measured from the tBLG at  $n_{BLG} = 0$  and  $D_{BLG} = -90$  mV/nm.

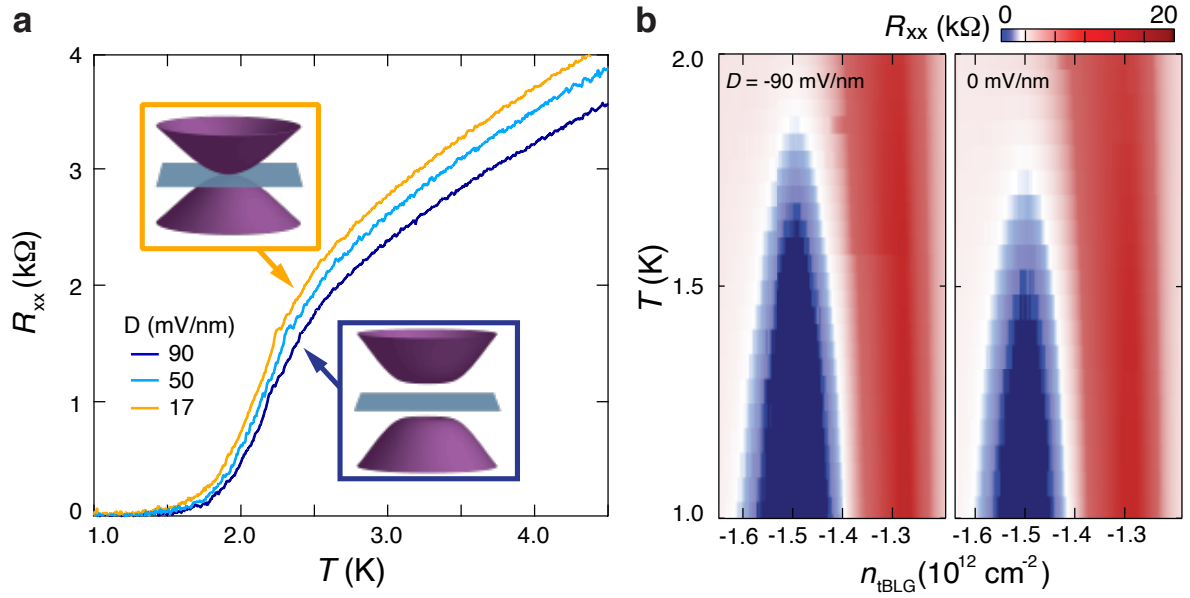


Fig.SI 6. (a)  $R_{xx}$  versus  $T$  for the superconducting phase at optimal doping, measured at  $n_{BLG} = 0$  with different  $D$ . (b)  $R_{xx}$  as a function of  $T$  and  $n_{tBLG}$ , measured at  $n_{BLG} = 0$  with different  $D$ .

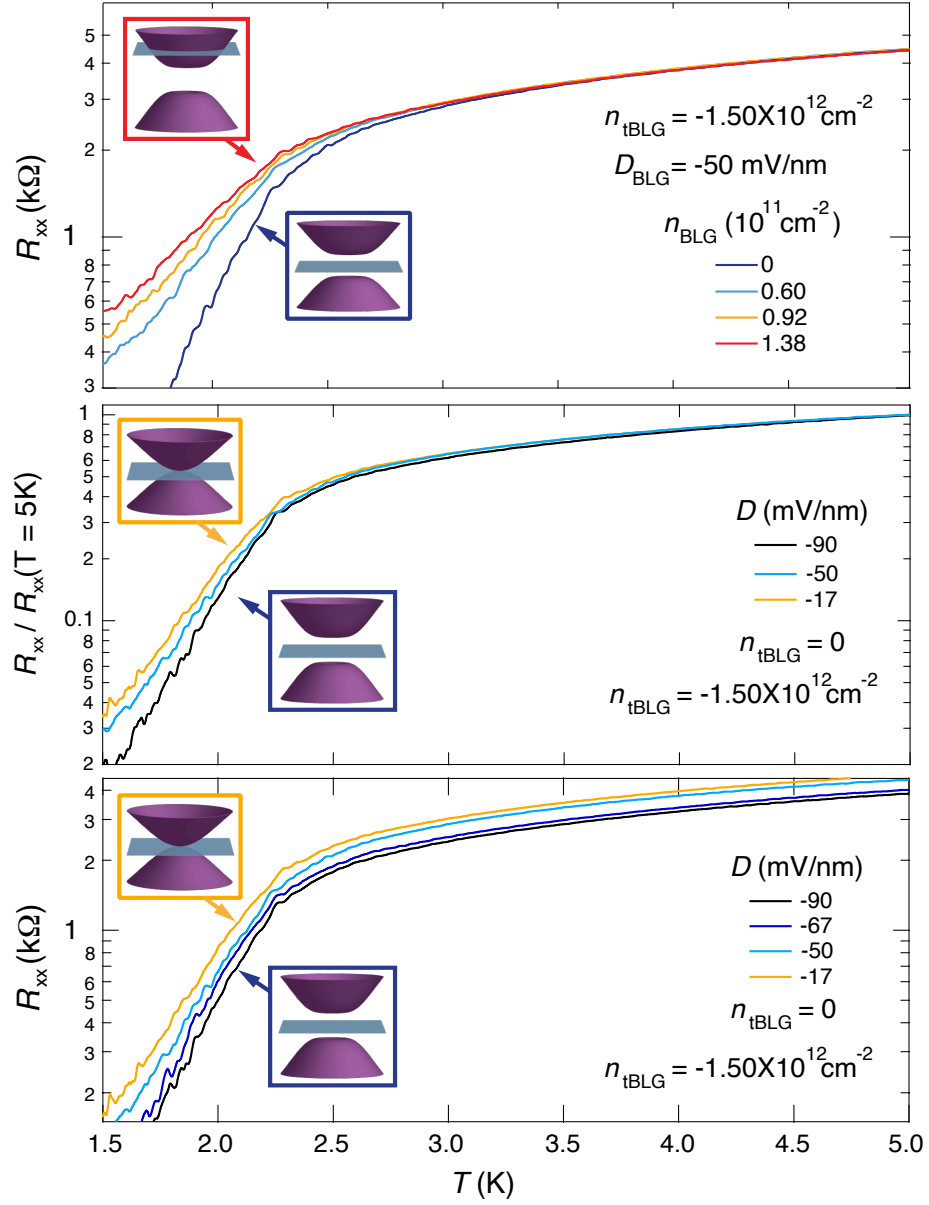


Fig.SI 7.  $R_{xx}$  versus  $T$  for the superconducting phase at optimal doping, measured at (a)  $D_{BLG} = -50$  mV/nm and different  $n_{BLG}$ ; (b) and (c)  $n_{BLG} = 0$  and different  $D_{BLG}$ .  $R_{xx}$  is normalized to its value at  $T = 5$  K in panel (b). The systematic shift in the temperature dependence of  $R_{xx}$  indicates that the relative change in  $T_c$  is independent of how  $T_c$  is defined.

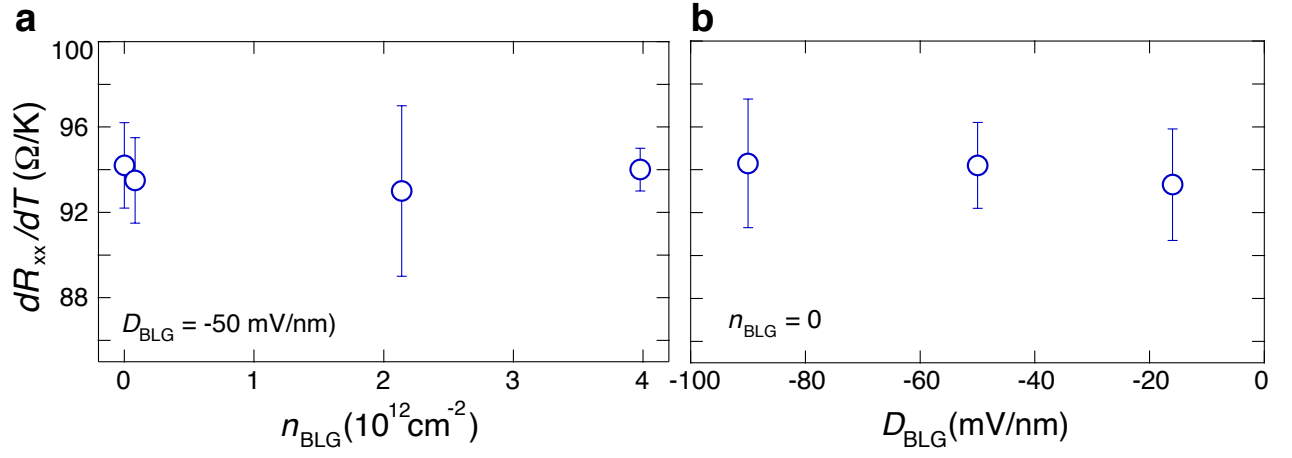


Fig.SI 8. The slope of  $R_{xx}$  in the T-linear regime as a function of (a)  $n_{BLG}$  and (b)  $D_{BLG}$ . When BLG is tuned over this range of parameters, the variations in the energy gap of CI and  $T_c$  of the superconducting phase are around 30% and 10%, respectively. In comparison, there is no detectable variation in  $dR_{xx}/dT$ .

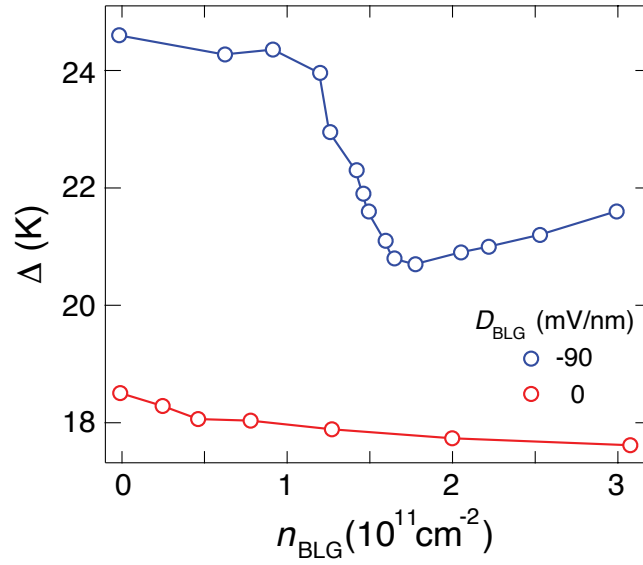


Fig.SI 9.  $\Delta_{\nu=2}$  as a function of  $n_{BLG}$  measured at  $D_{BLG} = 0$  and  $-90 \text{ mV/nm}$ . At  $D_{BLG} = 0$ , weak tunability in  $n_{BLG}$  is observed. On the other hand, in the presence of a large energy gap induced by  $D_{BLG} = -90 \text{ mV/nm}$ ,  $\Delta_{\nu=2}$  displays significantly larger variation as BLG transitions from fully insulating to conductive.

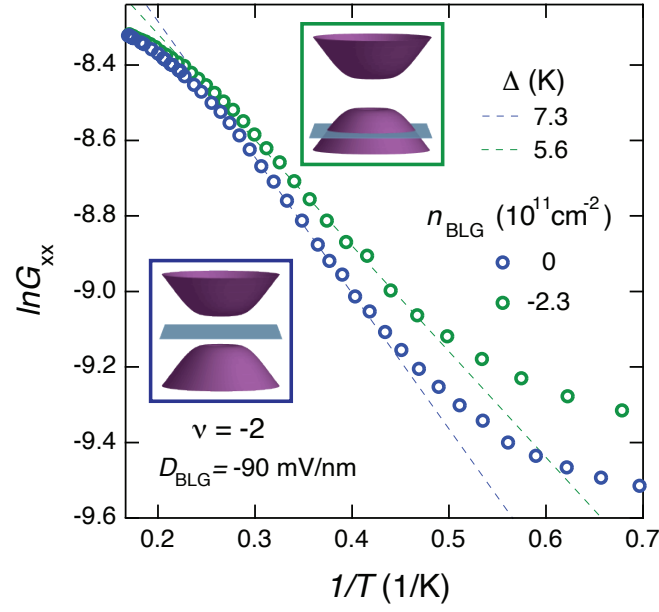


Fig.SI 10. Arrhenius plot for the CI at  $\nu = -2$  measured at  $D_{BLG} = -90$  mV/nm with different carrier density in BLG. A larger energy gap is observed when BLG is insulating with  $n_{BLG} = 0$ , compared to when BLG is conductive at  $n_{BLG} = -2.3 \times 10^{11}$  cm $^{-2}$ .

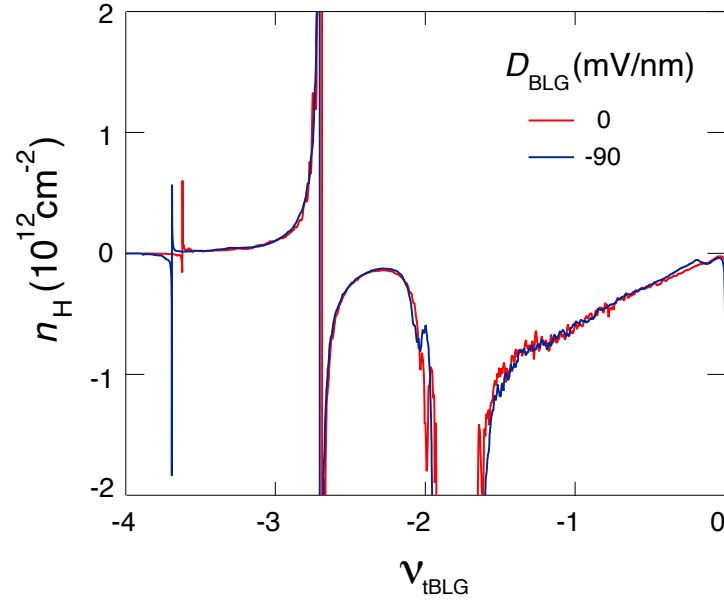


Fig.SI 11. Hall density  $n_H$  as a function of  $\nu_{tBLG}$  measured at  $B = 0.15$  T,  $n_{BLG} = 0$  with different  $D_{BLG}$ . The Hall density resets to zero at  $\nu = -2$ , indicating the formation of a new, small Fermi surface. The behavior of Hall density is insensitive to Coulomb screening from BLG, suggesting that the tunability to the CI and the superconducting phase does not result from changes in Fermi surface reconstruction near  $\nu = -2$ .



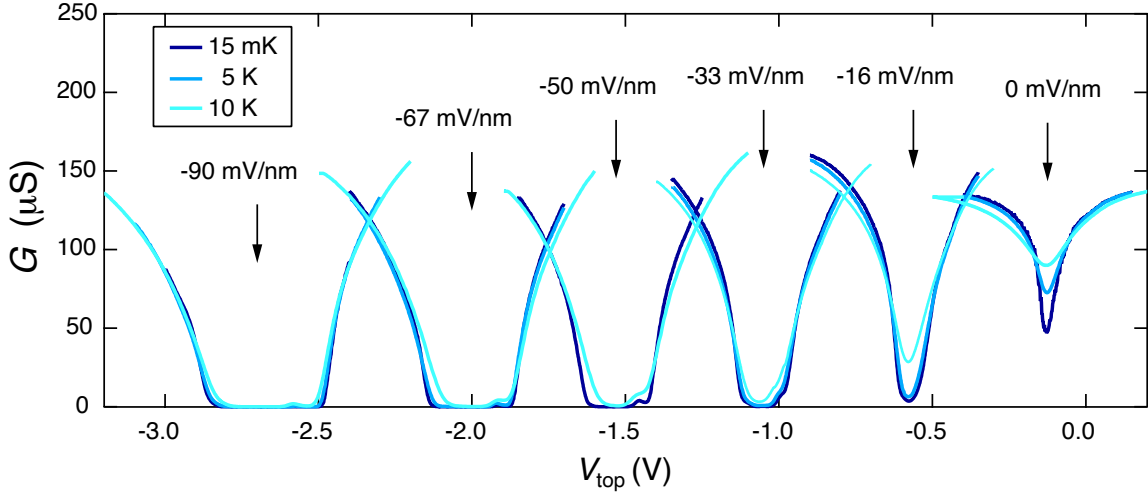


Fig.SI 12. Conductance of BLG as a function of  $V_{top}$  measured at different  $D$  and  $T$ . For  $|D| > 16$  mV/nm, the conductance of BLG remains constant up to 5 K. For  $|D| > 30$  mV/nm, the conductance of BLG remains constant up to 10 K. As a result,  $\Delta_{\nu=2}$  and  $T_c$  measurements in tBLG reported in this work are not influenced by the temperature dependence of BLG.

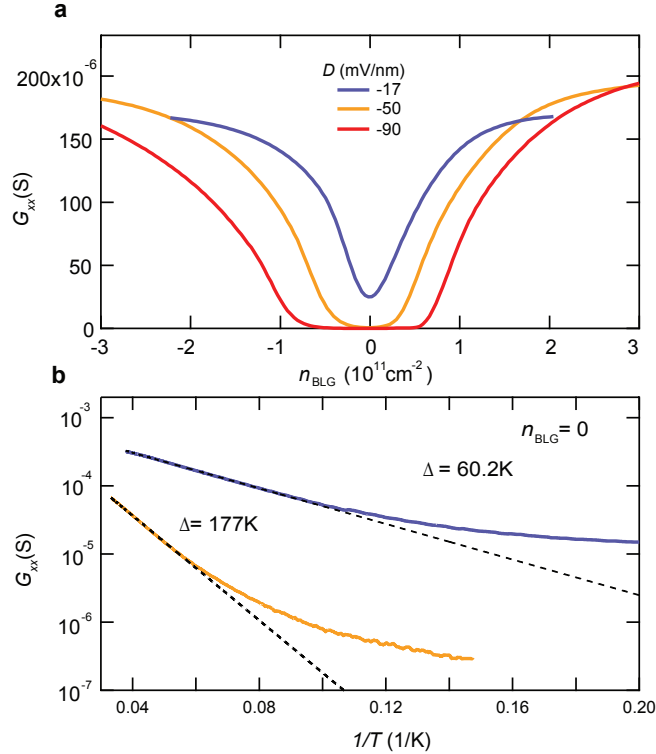


Fig.SI 13. (a) Conductance of BLG as a function of  $n_{BLG}$  measured at different  $D$  and  $T = 15$  mK. (b) Arrhenius plot measured in BLG, showing the amplitude of energy gap near the CNP at different  $D_{BLG}$ . The energy gap at  $D = 90$  mV/nm is much larger than 177 K. It is not shown here due to the high temperature range required for such measurement.